Thrust Vectoring of Small-scale Solid Rocket Motors Using Additively Manufactured Jet Vanes

Josef Biberstein*, Ezra Tal† and Sertac Karaman‡
Massachusetts Institute of Technology, Cambridge, MA, 02139

Small-scale thrust vector control (TVC) has the potential to enable rocket-powered micro aerial vehicles (MAV) capable of extremely fast and agile maneuvers. Jet vane TVC systems are particularly suitable for this task as they are capable of roll control and of exerting large side forces and moments at low airspeeds where aerodynamic surfaces are ineffective. In this paper, we present a novel small-scale TVC design using servo-actuated jet vanes. Our proposed design attains affordability and ease of manufacturing through use of modern additive manufacturing techniques. Titanium jet vanes are fabricated using selective laser sintering (SLS), and a ceramic heat shield, fabricated using stereolithography (SLA), is also designed. We evaluate the aerodynamic and thermal performance of the proposed design through numerical simulations, including modeling of rocket exhaust composition, computational fluid dynamics (CFD), and conjugate heat-transfer. Additionally, we present a test stand that enables measurement of forces and moments under both static and dynamic jet vane inputs. An initial static fire test is conducted using four vanes arranged in X-formation in the exhaust of a 54 mm commercial solid rocket motor. Experimental results are presented and compared to our numerical simulations.

I. Introduction

Jet vanes are aerodynamic vanes that are inserted into the exhaust of a propulsion system to generate side forces and moments by deflecting the flow. By controlling these forces and moments through the angle of attack of the jet vanes, thrust vector control (TVC) is achieved. In the field of rocketry, they are one of the earliest methods used to attain TVC — graphite jet vanes were used, in addition to external aerodynamic vanes, as the TVC solution on the original V2 rocket [1]. More recently, jet vanes have been used on missiles to obtain large control forces at relatively low airspeed, where aerodynamic surfaces are less effective [2]. Their ability to provide large forces makes jet vanes particularly suitable for agile maneuvers, such as fast pitch-over directly after launch and terminal guidance with large accelerations [2, 3]. The effectiveness and attainability of jet vane TVC has also been demonstrated in amateur rocketry, where it has been applied for stabilization during ascent [4]. These qualities make jet vanes a promising solution to perform aggressive vectoring for an autonomous micro aerial vehicle (MAV) powered by a solid rocket motor.

Applied research in the fields of robotics and autonomy makes extensive use of MAVs. In particular fixed-wing aircraft and rotorcraft, such as multicopters, have seen wide adoption. Their popularity can be attributed in part to the relative ease with which custom vehicles can be designed and fabricated using cheap, off-the-shelf components. In recent years, the increasing availability of additive manufacturing, or *3D printing*, has enabled further customization of these aircraft [5, 6]. Miniature rocket-powered vehicles, such as small sounding rockets and model rockets, may be more challenging to leverage for robotics and autonomy research as the high energy density of their propulsion requires special consideration in design and manufacturing. However, the combination of jet vane TVC with a small-scale solid rocket motor (i.e., impulse class I through K) has the potential to enable extremely fast and agile flight maneuvers. A rocket-powered research platform would be able to attain much higher speed and acceleration than most current platforms, posing exciting challenges for robotics and autonomy hardware and algorithms. In this work, we investigate the use of additive manufacturing to enable effective and affordable jet vane TVC of small-scale rocket motors. This combination of 3D printing and hobby-grade rocket propulsion can potentially be leveraged to make highly-maneuverable, rocket-powered MAVs more attainable.

This work contains several contributions. Firstly, we present our novel TVC system, including additively manufactured jet vanes and servo actuation, which can be directly integrated into a vehicle design. As far as we are aware, this is the first system that leverages 3D printing to attain compact and cost-effective jet vane TVC. Secondly, we perform a

*Graduate Student, Department of Aeronautics and Astronautics, and Laboratory for Information and Decision Systems, AIAA Student Member.
†Graduate Student, Department of Aeronautics and Astronautics, and Laboratory for Information and Decision Systems, AIAA Student Member.
‡Associate Professor of Aeronautics and Astronautics, Laboratory for Information and Decision Systems, AIAA Senior Member.

comprehensive numerical analysis, including modeling of exhaust composition and aerodynamic and thermodynamic analysis, to estimate the performance of the proposed system. Thirdly, we present a hot fire testing apparatus that enables measurement of forces and moments exerted by our proposed jet vane TVC system under both static and dynamic jet vane inputs. Fourthly, we provide preliminary experimental results from a hot fire test using the proposed TVC system in combination with a solid rocket motor. This experiment serves as a point of comparison for our numerical models and to evaluate both the effectiveness of the proposed TVC system and the structural robustness of the 3D printed jet vanes when exposed to the rocket exhaust stream for the test duration.

II. Jet Vane Design Using Additive Manufacturing

We consider the design of a jet vane TVC system for a small-scale rocket motor based on a typical four-vane configuration, (i.e., four jet vanes arranged radially around the rocket nozzle at 90° intervals). The design concept is presented in Figure 1, along with the coordinate system and jet vane numbering. We define the pitch angle, or angle of attack, of each jet vane such that a positive value corresponds to counter-clockwise rotation when viewed from the inside of the mounting tube. By moving pairs of opposite-located jet vanes together (i.e., with opposite pitch angles), the lift on the pair of vanes produces a side force on the mounting tube without producing a rolling moment around the z-axis. Similarly, opposite-located jet vanes with identical pitch angle produce no net side force, but will produce a rolling moment. At large angles of attack, jet vanes are able to produce larger side forces than other TVC methods, such as motor gimballing. However, large angles also decrease the overall motor thrust due to drag forces on the vanes.

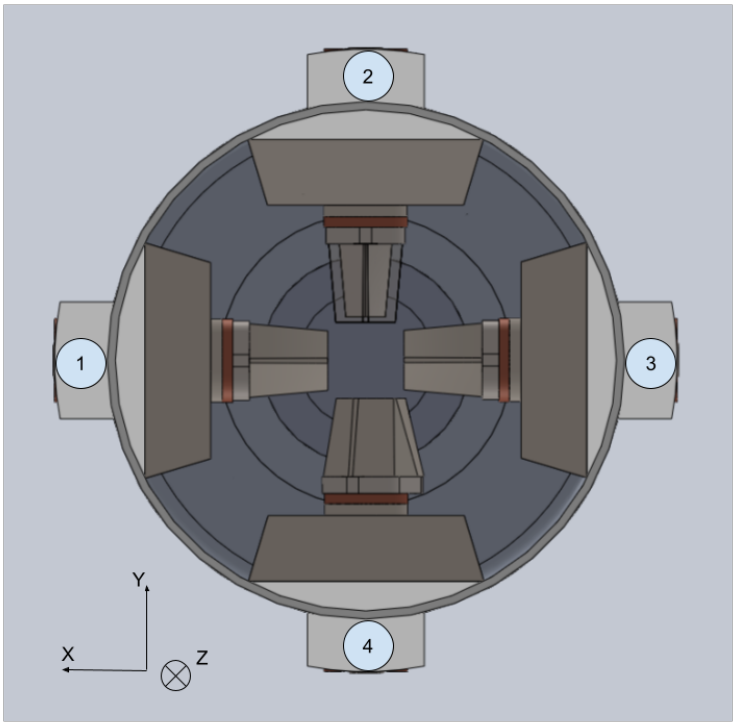

Fig. 1 Layout of the jet vanes. Vane 4 is at a 15° angle of attack and vane 2 has a transparent sheath to show the core piece.

Jet vanes must operate in the exceedingly harsh environment of the solid rocket exhaust stream which, even for small-scale solid rocket motors, can reach over 1000 K and Mach 2 at the nozzle exit. In addition, condensed phase matter in the exhaust can cause significant erosion of the vanes during the burn. As such, refractory metals, particularly copper-infiltrated-tungsten (CIT), are often used to construct jet vanes because of their combination of structural robustness and thermal conductivity [7–9]. Nonetheless, even a CIT vane may incur significant erosion — as much as 8 % mass loss during exposure to the burn of a motor with an 9 % aluminum content has been observed [7]. While the commercial hobby-rocketry motors considered in this study have lower metal contents (around 5 % or lower), significant

erosion is still expected. Liquid rocket engines permit the use of less erosion-resistant materials, because of the absence of significant amounts of condensed phase matter in their exhaust. In this case, non-metals with a high melting point, such as graphite, provide superior thermal performance [4]. However, our focus on simplicity and affordability precludes the use of liquid propulsion.

Prior work has shown the efficacy of jet vanes manufactured subtractively. However, even for simple vane designs, subtractive techniques can be relatively expensive, requiring 5-axis computer numerical control (CNC) machining to produce high-quality parts. This cost is further exacerbated by the aforementioned erosion effects, which typically necessitate replacement of the vanes after each firing. In order to design a jet vane TVC system suitable for small-scale rockets, we examine wide-spread additive manufacturing technologies to produce vanes cheaply and in a way that may better support multiple firings. We consider two jet vane designs, both manufactured additively. The first jet vane design is fabricated completely out of 3D-printed titanium. The second design consists of two 3D-printed parts: a titanium core and a silica ceramic heat shield that we refer to as the *sheath* of the jet vane. In the second design, the titanium core provides the strength necessary to bear the side forces generated by the vanes, while the silica sheath provides a layer of insulation that keeps the titanium core below its melting temperature and protects it from erosion. As such, the titanium core can be reused through multiple firings, while only the sheath must be replaced due to erosion. While the use of a (zirconia) ceramic coating for jet vanes has been considered in existing work [10], our proposed design is the first purely 3D-printed architecture that we are aware of.

The titanium components, (i.e., the entire first design and the core of the second design), are 3D-printed out of Titanium Grade 23 using selective laser sintering (SLS). The sheath is fabricated out of a silica ceramic resin using stereolithography (SLA) and then sintered in a kiln. The use of additive manufacturing greatly reduces the cost of both the sheath and the core. While the final cost depends on the exact printing specifications, the price for a custom set of four titanium cores and four ceramic sheaths will be on the order of several hundred US dollars, when ordered from a commercial 3D-printing service. The finished core and sheath components can be seen in Figure 2.

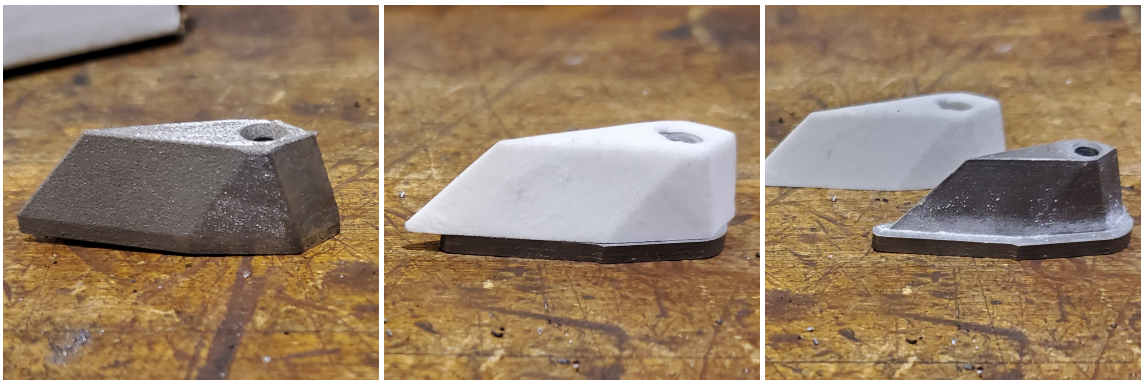

(a) Titanium vane. **(b) Titanium vane core with sheath attached.** **(c) Titanium vane core with sheath removed.**

Fig. 2 3D printed jet vane components

We use a diamond wedge shape, as is often done for supersonic airfoils, with the addition of a taper to increase the incidence angle of condensed phase particles colliding with the leading edge of the vane. The increased incidence angle alleviates erosion at the leading edge. The span l_{jv} of the vanes is 11.91 mm and the planform area A_{jv} is 4.19 cm^2. Currently, these dimensions are mainly imposed by space constraints with respect to fitting the TVC units in a mounting tube with 3 inch inner diameter. However, the aerodynamic performance of the vane may be improved in future iterations through optimization of its geometry.

A computer-aided design (CAD) model of an individual TVC unit can be seen in Figure 3. The jet vane is mounted on a stainless steel shaft that is actuated by a servo motor via an external gearbox. A larger gear ratio increases the maximum holding torque of the servo, but also reduces the effective speed of the servo at the vane shaft. Consequently, the choice of servo motor and gearing ratio presents a trade-off between maximum vane angle of attack, and minimum response time to angle commands. This trade-off is discussed more in Section III.B.

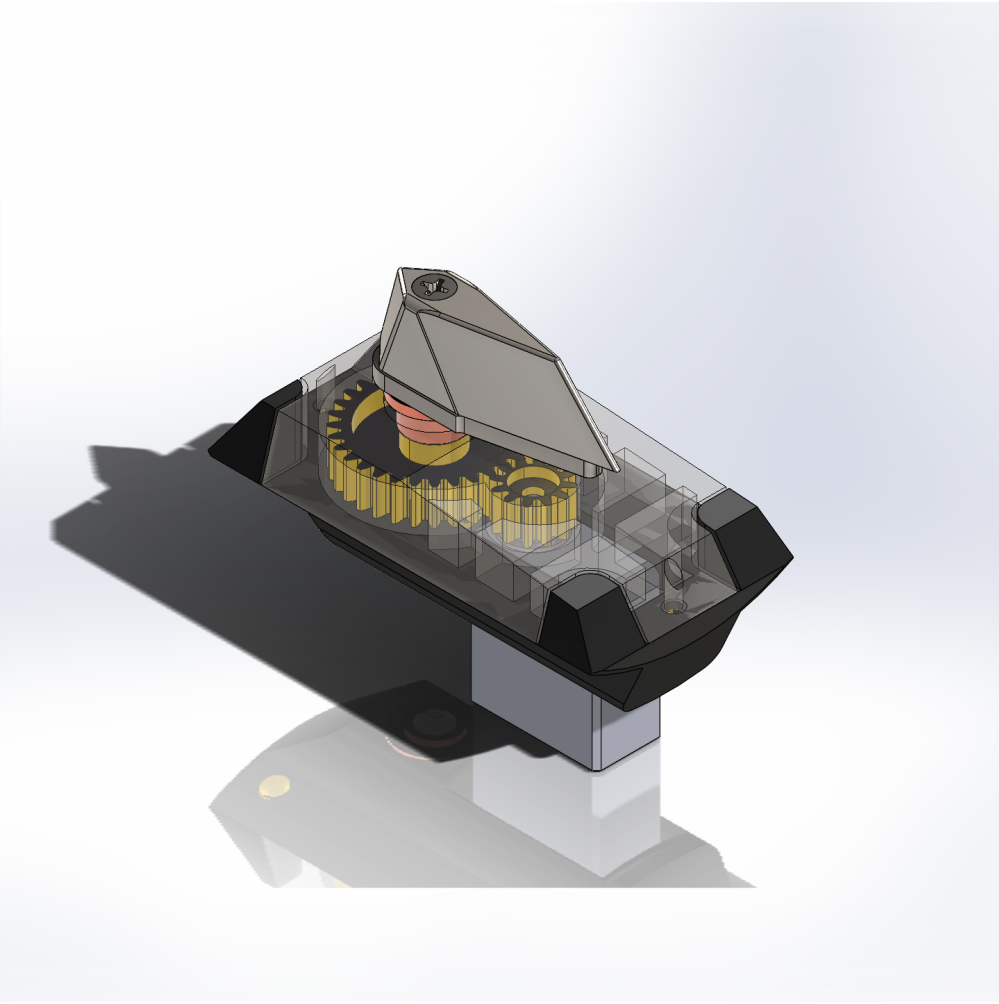

Fig. 3 CAD model of a TVC unit.

III. Numerical Analysis

We predict the aerodynamic and thermal performance of our vane designs using CFD simulation based on the FlowEFD solver (via SolidWorks Flow Simulation). For both the thermal and aerodynamic analyses, the ambient conditions are assumed to be sea-level standard. The significant interaction between the vanes can account for as much as a 60 % increase in vane loading [11]. Consequently, all four vanes must be included in the computational model. The problem geometry is shown in Figure 4. We note that openings are made in the holding tube between each TVC unit to reduce shrouding losses. Without such openings, directing the flow into the mounting tube creates adverse aerodynamic forces which reduce the effectiveness of the vanes [10]. We note that the design of our test stand, discussed in IV, does not permit such openings. Hence, we expect reduced performance of the vanes in the test stand due to increased shrouding effects.

In order to accurately simulate the rocket exhaust, a representative exhaust model is developed commensurate with the chemistry of a typical small-scale hobby rocket motor, as described in Section III.A. An inlet condition in the normal direction to the motor nozzle exit plane is included to expel the representative exhaust at Mach 2.5, 1300 K, and atmospheric pressure. These conditions were chosen based on publicly available data from static fire tests of commercial propellant grains similar to those used in our tests [12]. We perform four unsteady conjugate heat transfer simulations of four-second burns: one for each of our two designs (i.e., solid titanium and titanium with ceramic sheath) at both 0° and 30° angles of attack. Additionally, steady-state simulation is used to estimate the lift and drag coefficients for a single vane in several scenarios and to estimate the side force produced by two vanes pitching together. The results of these simulations serve to validate our vane design and as a point of comparison for the static fire test.

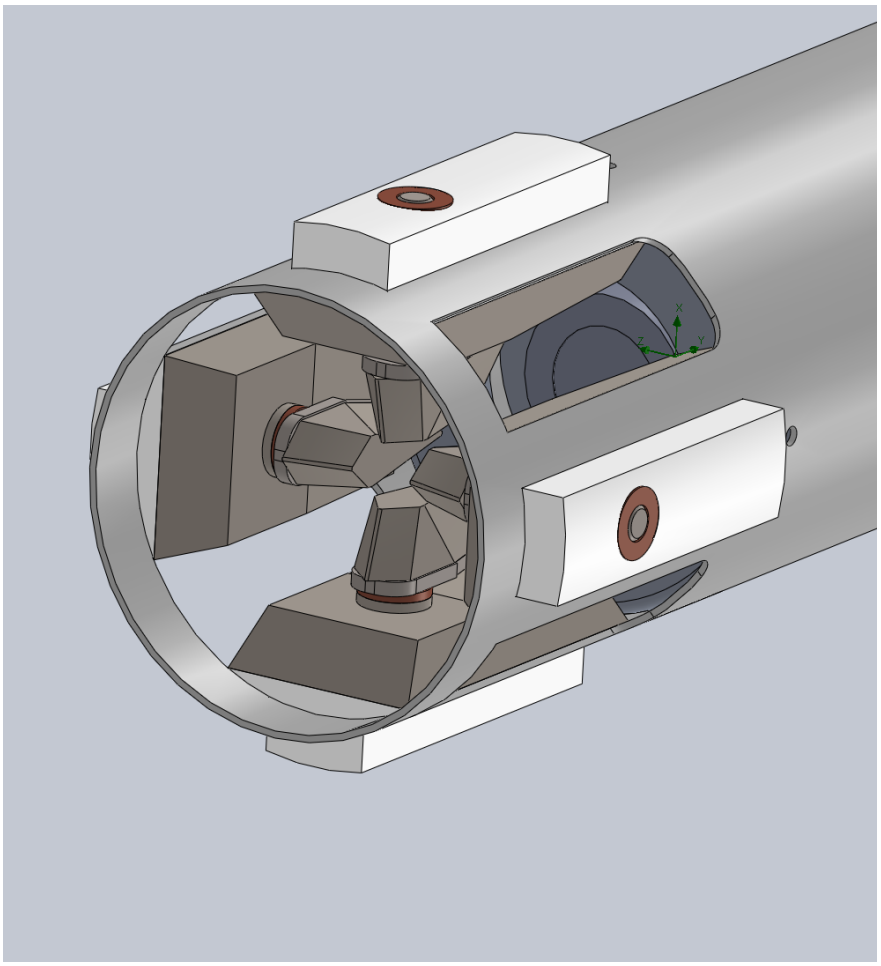

Fig. 4 Defeatured geometry used for CFD simulations. Vane angles are varied for different simulations.

A. Representative Rocket Exhaust Chemistry

In order to accurately simulate the performance of our jet vane design using CFD, we define a representative exhaust gas which results from a representative motor chemistry similar to what would be found in small rocket motors. We then determine the thermal and transport properties of this exhaust gas at a range of temperatures commensurate with what we expect to see in the static fire test. For this work, a representative motor chemistry of 75 % ammonium perchlorate (AP), 20 % hydroxyl-terminated polybutadiene (HTPB), and 5 % aluminum was selected. Since the formulas of the commercial 54 mm motors that we use in this study are not publicly available, this chemistry represents a worst-case estimate of the metal content. This is done because a high metals content is the main driver of condensed phase matter in motor exhaust products, which in turn is the main driver of erosion of jet vanes during the burn. With this in mind, we expect the comparatively low metals content common in hobby motor formulas to be an advantage inherent to our application which will reduce the effects of erosion. While 5 % is low for many formulas considered for missiles, it is commensurate with small hobby scale motors for which the residency time of the exhaust gas in the motor core is comparatively low. A low residency time prevents large amounts of aluminum from combusting completely and providing increased specific impulse. Therefore, low metal formulas are used by hobbyists.

This composition was used as input to the Rocket Propulsion Analysis [13] software which uses a Gibbs free energy minimization approach to obtain the resulting combustion products given in Table 1. We note that some species appearing in small concentrations (less than 0.0001 % in total) in the resulting gas were neglected. The combustion was calculated at a chamber pressure of 6.9 MPa (1000 psi) and a temperature of 2366 K. These values were estimated using publicly available data from tests of commercial rocket motors used in hobby rocketry [12]. This composition was then used to construct a model of the gas in the open source chemical kinetics software Cantera [14] from which the transport properties of the gas could be obtained. The calculated transport properties over a range of temperatures are given in Figure 5 and are used as an input to FLowEFD to accurately represent the exhaust.

Species	Mass fraction	Molar fraction
CO	0.2918807	0.2311016
H2	0.0309176	0.3401366
H20	0.0873131	0.1074857
N2	0.0909298	0.0719868
HCl	0.2327513	0.1415718
CH4	0.0006979	0.0009648
CO2	0.1710176	0.0861800
Al2O3(a)	0.0944733	0.0205488
Total	**0.9999813**	**0.9999761**

Table 1 Representative rocket exhaust composition.

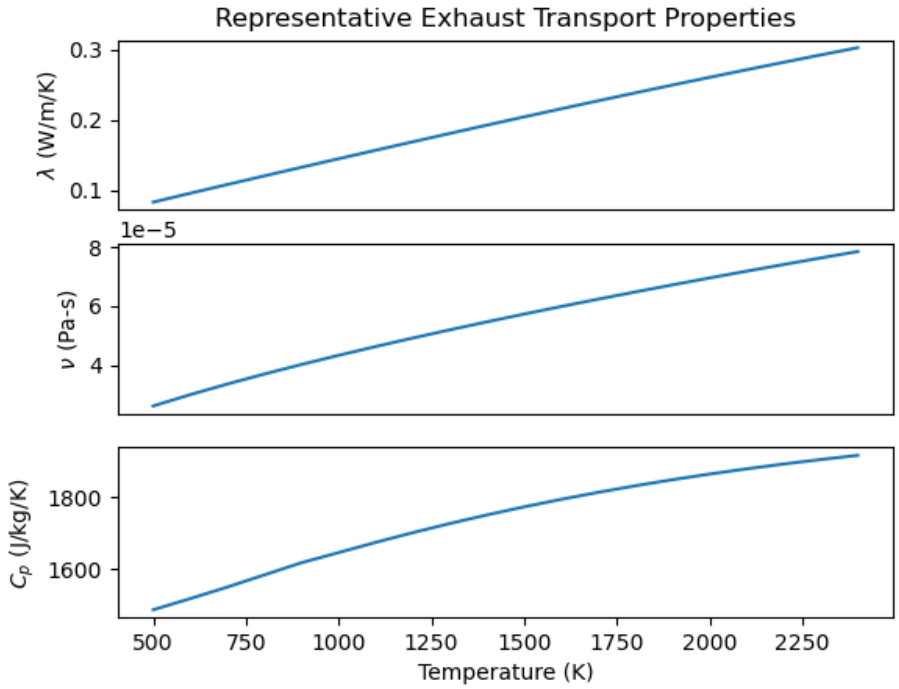

Fig. 5 Transport properties for representative rocket exhaust. λ gives the thermal conductivity, ν gives the dynamic viscosity, and C_p gives the specific heat capacity.

B. Aerodynamic Performance

Lift, drag, and pitching moment coefficients are calculated for vane 1 in several different scenarios. The results can be seen in Figure 6. The coefficients are calculated as follows

$$C_L = \frac{L_{jv}}{q_{ex} A_{jv}} \tag{1}$$

$$C_D = \frac{D_{jv}}{q_{ex} A_{jv}} \tag{2}$$

$$C_M = \frac{M_{jv}}{q_{ex} A_{jv} l_{jv}} \tag{3}$$

where A_{jv} is the planform area of the jet vane, l_{jv} is its span, and q_{ex} is the dynamic pressure sampled in the free stream of the exhaust near the nozzle exit plane. Values are calculated for angles of attack from 0° to 30° at 1.5° increments. In scenario 1, vane 1 is the only vane adjusted. In scenario 2, vane 1 and vane 3 are adjusted together (vane 1 clockwise and vane 3 counter-clockwise). In scenario 3, vane 1 is again pitched alone but with vane 4 held at a 15° angle of attack. In all three scenarios, we observe that the lift coefficient departs from a linear trend and begins to flatten out starting around 20° of angle of attack. This trend is in good agreement with the observations in [10]. We also note that the first two scenarios produce almost the same trend for the aerodynamic parameters of vane 1. From this we conclude that there is very little interaction between opposite sets of vanes. However, we do see some interaction in the third scenario due to the presence of vane 4 at a 15° angle of attack — the rate of increase of the drag on vane 1 appears to be slightly higher after about 10° of angle of attack.

The side force generated by the two vanes pitching in scenario 2 is also estimated in order to understand the maximum side force that can be produced. Values were again calculated for pitching angles from 0° to 30° in 1.5° increments. The results can be seen in Figure 7. We see that the maximum side force is around 30 N which is approximately 10 % to 20 % of the average thrust of the commercial motors considered for this work. We can also use the maximum side force to estimate the angular acceleration for a representative small-scale autonomous rocket powered vehicle. Consider a small rocket (cylinder and pointed nose cone) which is 0.5 m in total length. We assume a mass of 2.5 kg, a pitching moment of inertia of 0.25 kg m^2, and a center of mass location $\frac{1}{4}$ of the total length aft of the nose cone tip. From this, we calculate a maximum angular acceleration of 45 rad s^{-2} due to the maximum side force. This equates to a time of approximately 0.37 s to complete a 180° rotation. This gives us some estimate of the agility enabled by the jet vane TVC system.

We can also estimate the maximum achievable vane angle of attack based on our choice of gear ratio and servo motor. Our current design uses a gear ratio of $\frac{1000}{375}$ and a servo with a stall torque of approximately 0.255 N m. This translates to a maximum holding torque of approximately 0.680 N m. Comparing this to our simulation results, we conclude that we should not attempt more than a 12° vane angle of attack with the current servo and gear ratio.

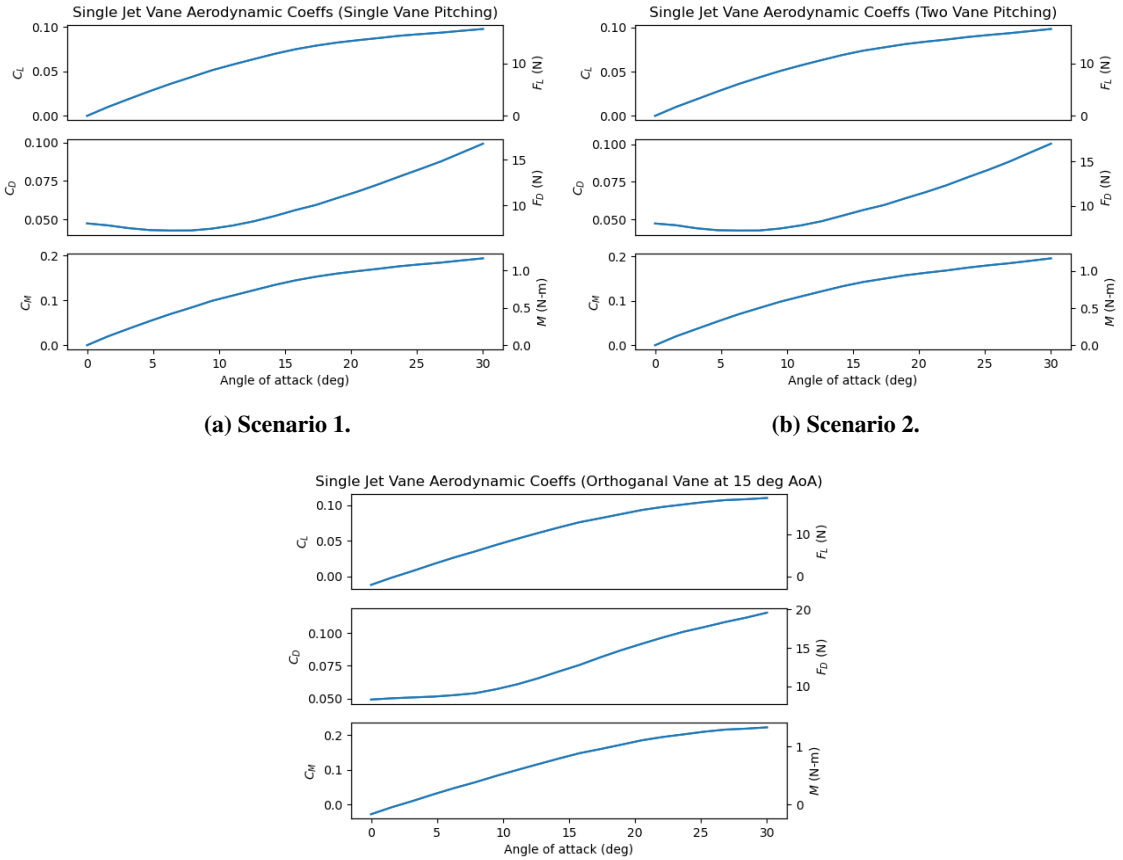

(a) Scenario 1.

(b) Scenario 2.

(c) Scenario 3.

Fig. 6 Calculated aerodynamic coefficients and associated force and moment magnitudes for vane 1.

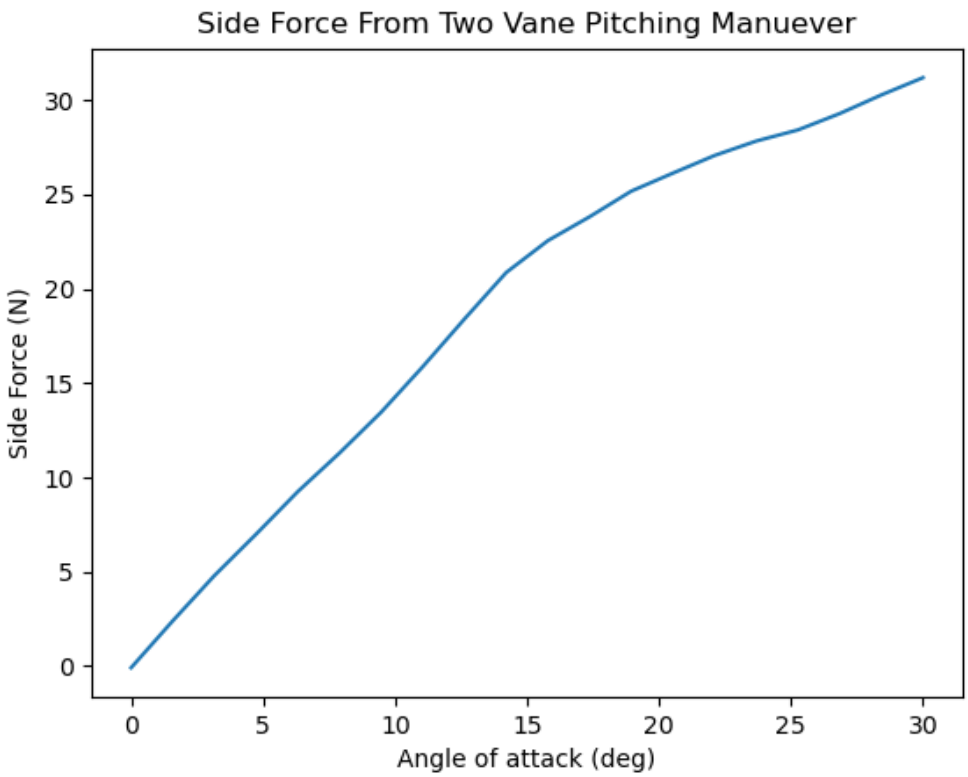

Fig. 7 Total side force produced in scenario 2.

C. Thermal Performance

In order to quantify the heating of the vanes during a four-second burn, an unsteady conjugate heat transfer (CHT) simulation in FlowEFD is used. Two meshes, one with the vanes all at 0° angle of attack and one with vane 1 at 30° angle of attack, are used. With both of these meshes, both the silica sheath with a titanium core, and a completely titanium vane are simulated.

Figure 9 shows a cut plot of the temperature of vane 1 at one-second intervals throughout the burn. As is expected, the low thermal conductivity of the silica causes heat to build up in the leading edge of the jet vane. This heats the silica beyond its melting point of 1986 K. We can therefore expect that the areas of the sheath that reach this temperature will ablate during the burn. However, at the end of the burn, the temperature of the titanium core is comfortably below its 1833 K solidus temperature. Figure 8a shows a surface plot of the silica sheath after the four second burn at 30°. The maximum temperature is again greater than the melting point of the silica, and thus the plot gives us an idea of where we might expect the most erosion of the sheath.

Figures 8d and 8b show the surface of a fully titanium vane at 0° and 30° of deflection respectively. We can see from the plots that the temperature of the titanium remains just below the solidus temperature. This indicates that the ceramic sheath may be unnecessary. However, the simulation may not be accurate enough to say with certainty that the titanium will remain below its solidus temperature in a real scenario. Additionally, there are several unmodeled effects that may adversely affect the vane at temperatures near its solidus. First, the tensile strength of Grade 5 Titanium, which is very similar to the Grade 23 Titanium used to produce our vanes, decreases significantly at high temperatures — some measurements show by up to 40 % [15]. Second, while the vanes used in this study are solid titanium, some metal additive manufacturing processes use internal scaffolding, similar to fused deposition modeling (FDM) printers, instead of printing a solid part. Decreases in yield strength may cause the internal structure of a printed titanium vane to buckle, deforming the vane. Therefore, keeping the temperature of the core as low as possible is advantageous.

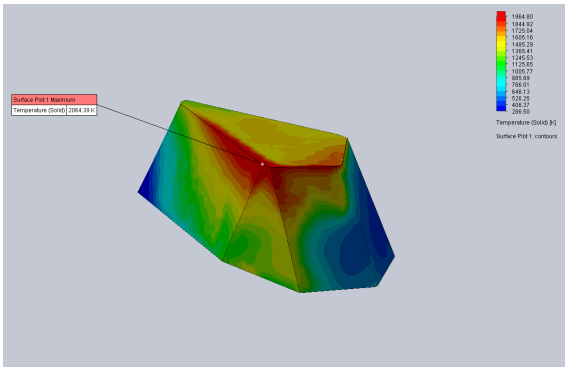

(a) Surface plot of silica sheath at 30° angle of attack

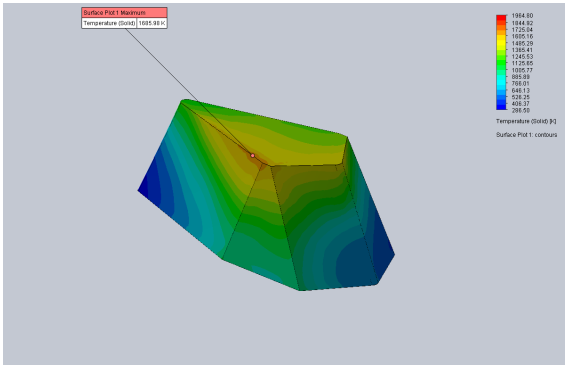

(b) Surface plot of solid titanium vane at 30° angle of attack

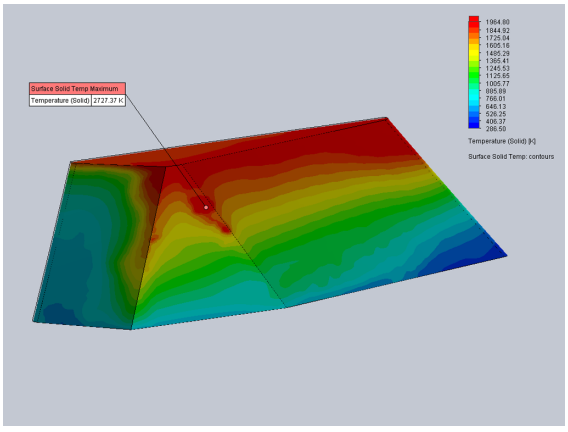

(c) Surface plot of silica sheath at 0° angle of attack

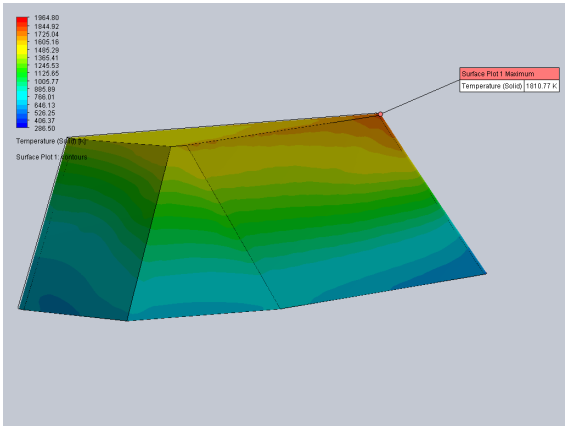

(d) Surface plot of solid titanium vane at 0° angle of attack

Fig. 8 Vane heating after four second burn for both silica sheath and titanium alone configurations

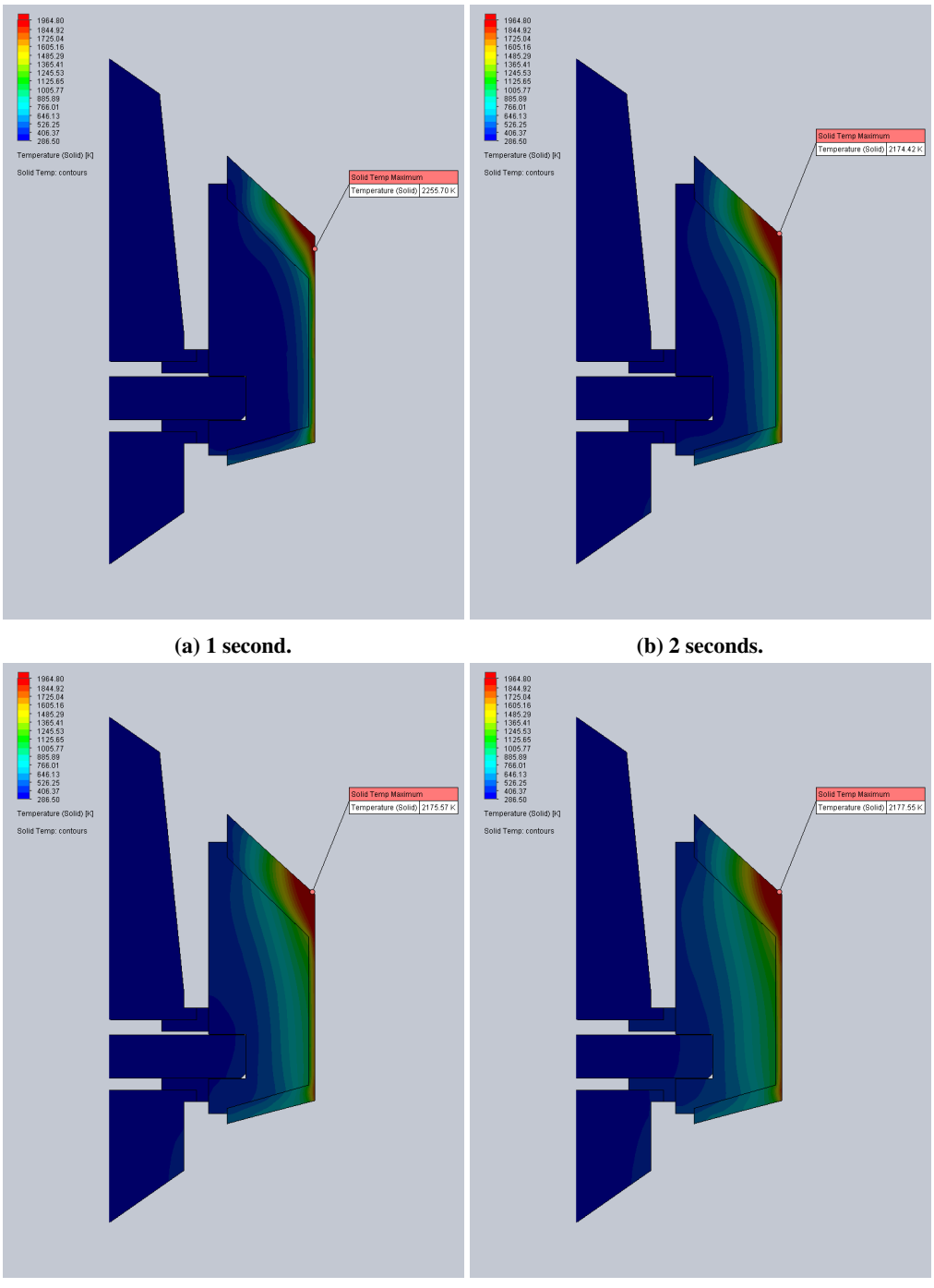

(a) 1 second. **(b) 2 seconds.**

(c) 3 seconds. **(d) 4 seconds.**

Fig. 9 Titanium-silica jet vane test article solid temperatures after exposure to rocket exhaust in a conjugate heat transfer simulation.

IV. Static Fire Experiment

In this section, we describe the results of an initial static fire experiment conducted using our proposed jet vane TVC units. This test serves to evaluate the ability of our jet vanes to produce useful side forces and as a point of comparison for the side forces calculated in simulation. The test is conducted with the solid titanium vanes, allowing us to qualitatively evaluate the amount of erosion the 3D-printed titanium design experiences. To conduct these experiments, a test stand is developed to accommodate a test article consisting of the previously discussed four-jet-vane setup and a 54 mm commercial rocket motor. The motor chosen for the test presented in this work is an I120 Imax motor from Ceseroni Technology*.

A. Test Stand Apparatus

The CAD for the test stand designed for this work can be seen in Figure 11 and the stand itself in Figure 10. It is capable of measuring side forces, axial force, and rolling moment on the test article. The total lift force produced by a given vane configuration can be deduced directly from the measured side forces. In addition, the total resulting drag can be deduced by calculating the difference between the measured axial force on the test article and the thrust curve provided by the motor manufacturer. The design uses an S-Type load cell (Figure 11c) in order to measure the axial load and six button load cells to measure the side forces and roll torque. Ball transfers are used to conduct load to the button type cells in order to minimize cross-talk between the measurement axes (Figure 11b). Bolts are used inline with the ball transfers to pre-load the cells and hold the test article in place. The S-type cell has a full-scale range of 50 kg and each button cell has a full scale range of 5 kg.

Data logging from the load cells is done with a Labjack T7. Each of the cells is sampled at a rate of 100 Hz. The servos in the TVC units are controlled by a Teensy 4.1 microcontroller. An interrupt is sent from the T7 to the Teensy when the measurement on the axial cell exceeds a certain threshold in order to trigger the start of a preprogrammed vane schedule.

B. Experiment Results

1. Vane Force Measurements

The total side forces, normalized by the measured thrust, in the vane frame of reference (see Figure 1) and the servo schedule used in the test are shown in Figure 12. The forces shown are computed using low-pass filtered data from the the test. The schedule followed by the vanes during the test is designed to mimic the simulation conditions The measured thrust produced by the motor during our test is compared to the thrust quoted by the manufacturer in Figure 13.

The servo schedule used in the test is divided into four distinct sections as indicated by the gray-white background pattern in Figure 12. Each of these sections is designed to mimic the scenarios used in the numerical simulations.

In the first section, all four servos are commanded to hold the vanes at a zero angle of attack. We note that there appears to be a small but noticeable increase in the side force in both directions during this stage. This is likely due to how the vanes are secured to the shaft — securing them axially to the shaft allows for some small amount of rotational freedom, even though the shaft has a flat edge to enforce clocking. This can be fixed in subsequent iterations of the design.

In the second section, vane 1 is commanded to move from 0° to 10° angle of attack linearly. As expected, we see the side force generated in the y-direction increase linearly as well. It is here that we see the maximum side force produced during the test: about 6 % of the measured motor thrust. This translates to a side force of about 7 N at a 10° vane angle of attack. This is slightly worse performance than was predicted by our simulations, where the trend was closer to about 1 N of side force per 1° vane angle of attack. However, as we also note previously, our test stand does not have openings in the test article to prevent shrouding losses. Therefore, some reduction in performance is expected.

In the third section, vane 1 is held at a 10° angle of attack and vane 2 is increased linearly from 0° to 10° angle of attack. We see a corresponding increase in the force in the x-direction, as expected. However, the increase is not as great as that seen in the y-direction in the second section. Furthermore, the force in the y-direction, which we would expect to be constant, shows a slight decrease. Both of these effects may be explained by a decrease in lift coefficient caused by the onset of erosion at this point in the burn.

In the fourth section, vanes 2 and 4 are pitched together in order to produce a greater total side force. We note the small drop in the side force in the x-direction observed at the beginning of this section which mirrors that seen in the

*Thrust data available at `https://www.thrustcurve.org/motors/Cesaroni/502I120-15A/`.

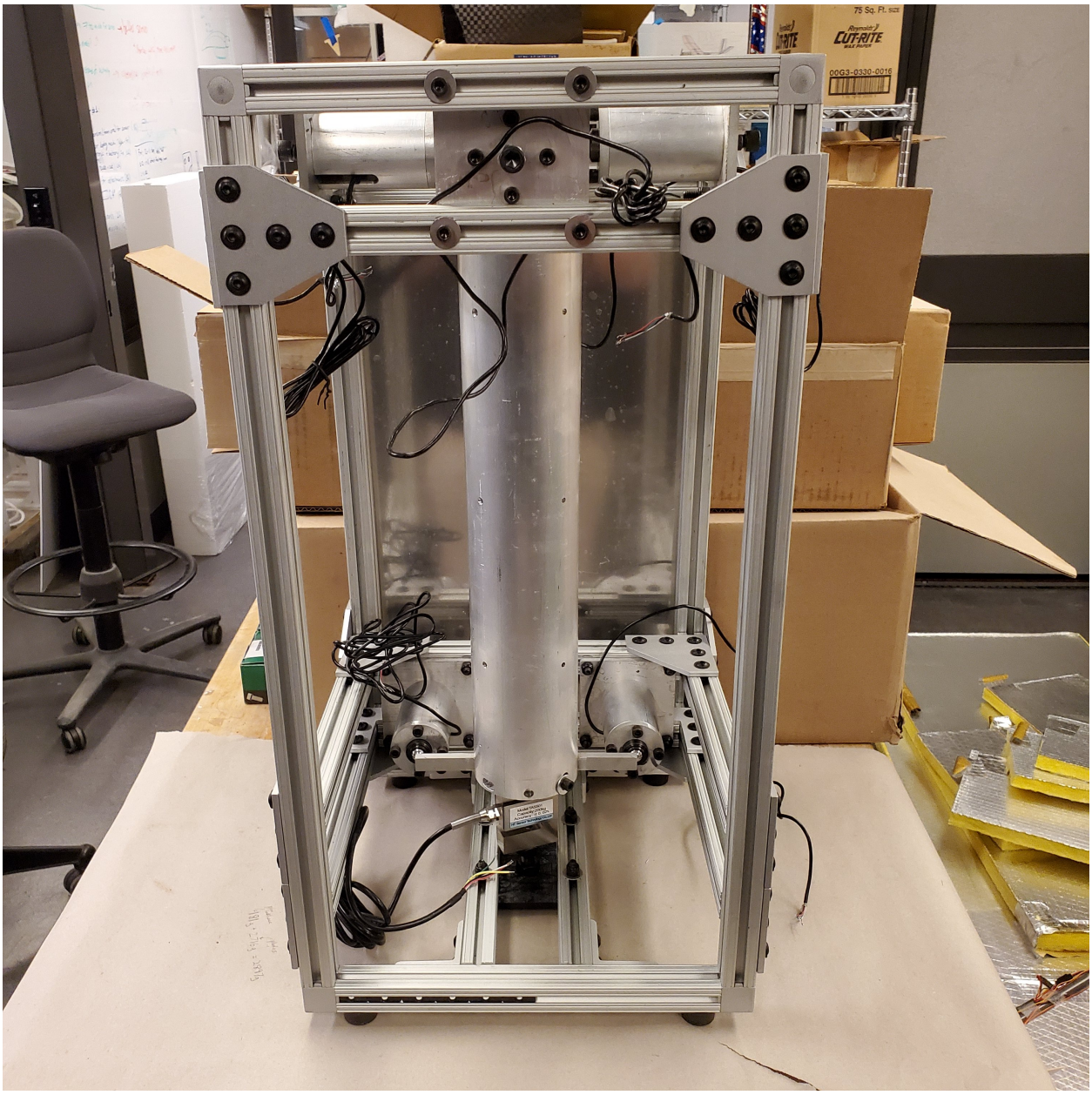

Fig. 10 Test stand designed for testing jet vane TVC units.

beginning of the first section. We can conclude that this may also be caused by the axial mounting of the vanes to the shaft. Taking this initial negative offset into account, we observe that the two vanes also produce a normalized side force of about 6 %. This is about half of what we might expect given the performance of vane 1 in the second section. The decrease in control authority may be attributed to erosion effects and to decreased exhaust velocity at the end of the motor burn.

As expected, the axial thrust measured during the test is lower than the quoted thrust from the motor manufacturer due to the drag produced by the jet vanes. One interesting feature to note is that, between 10 s and 12 s, the gap between the two thrust curves grows larger. This corresponds to the period in the servo schedule when the vanes begin to adjust to higher angles of attack. However, in the period of the test after about 12 s, the gap between the two curves shrinks again to about the same magnitude as in the period from 9 s to 10 s. This is further evidence that significant vane erosion had occurred at this point in the test, dropping the drag coefficients of the vanes.

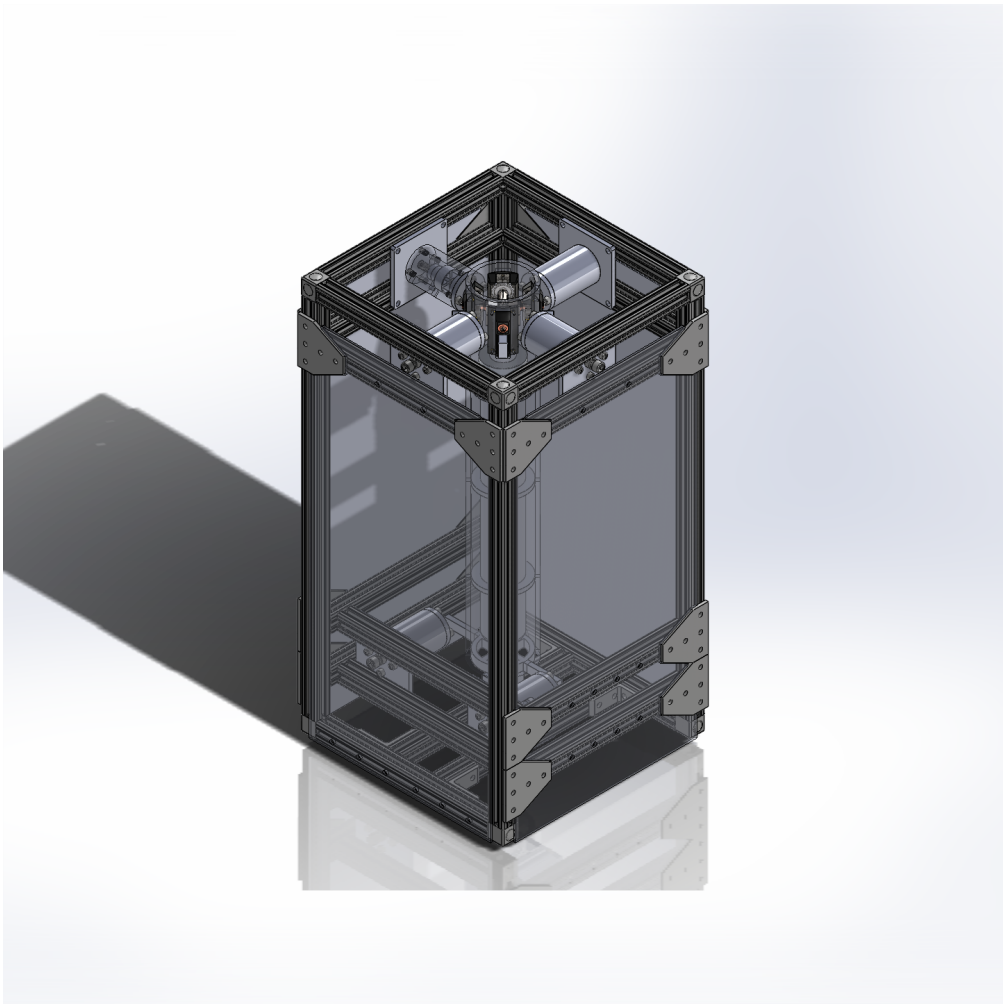

(a) CAD model of jet vane test stand.

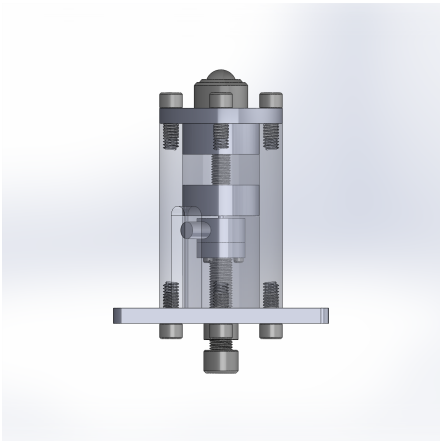

(b) Linear force transfer apparatus for measuring side forces.

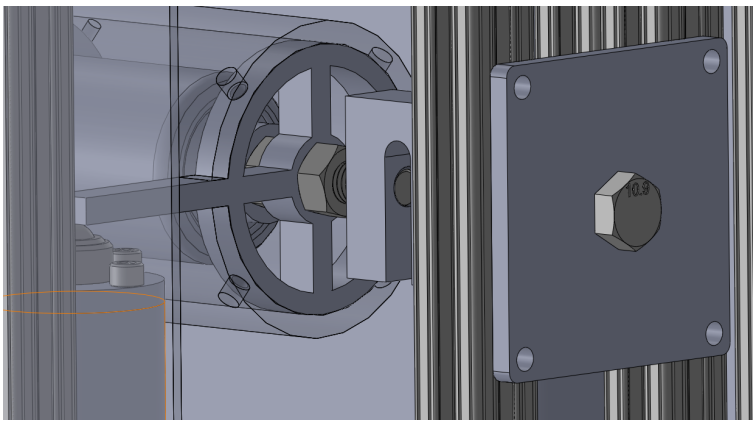

(c) Thrust and roll measurement instrumentation.

Fig. 11 CAD model of test stand and views of instrumentation.

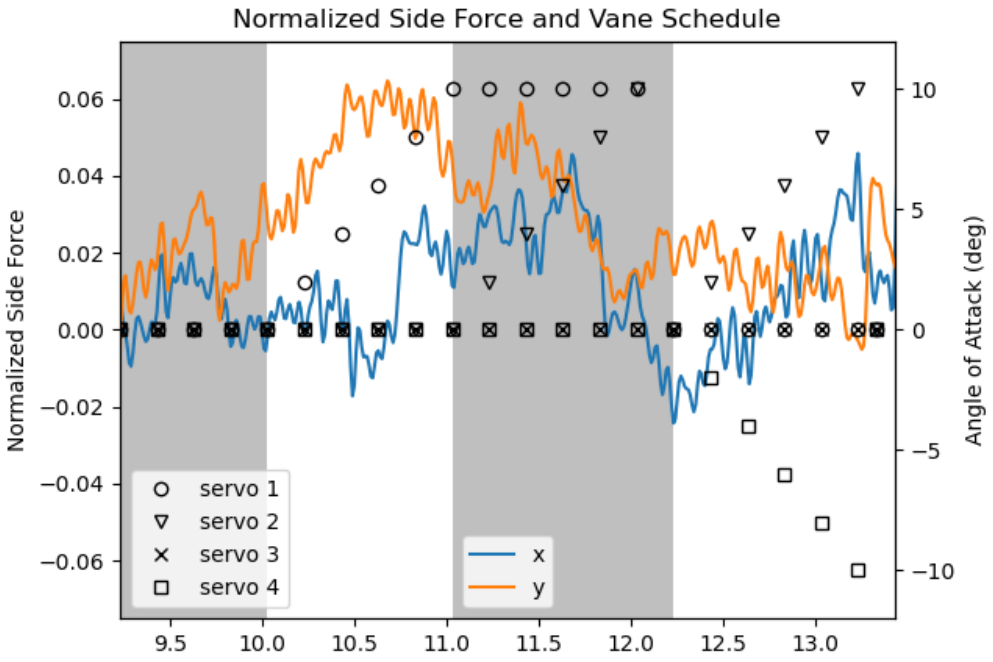

Fig. 12 Normalized side forces exerted by jet vanes during test. Plotted against servo schedule. Side force data is low-pass filtered.

2. Vane Erosion

Figure 14 shows all four titanium vanes post-firing. It is clear that every vane exhibits some erosion. We also see that the erosion occurs starting on the leading edge at the top side of the vane. This matches the area with greatest temperature in our conjugate heat transfer simulation of the titanium vanes, offering additional support for our earlier prediction that the temperature would be a good proxy for where erosion would occur on the vane.

We can also note that, on some of the vanes, material was not completely eroded but was instead deformed. This is particularly obvious on vane 2, where rippling patterns can be seen on the top edge where the titanium melted and re-solidified. This observation suggests that the temperature of the titanium at the leading edge did not significantly exceed the solidus temperature, showing that our simulation underestimates the temperature of the titanium vane at the leading edge, but not egregiously so. This is additionally supported by measurements of the mass loss for each vane during the test, which shows a maximum of 3 % across all vanes measured (vane 4 was excluded because the shaft could not be removed). We also observe that vane 2 and 4 have the most visible erosion and deformation. This may be caused by the fact that these vanes were commanded to a large angle of attack near the end of the burn, when the temperature of the vanes would have been near or exceeding the solidus.

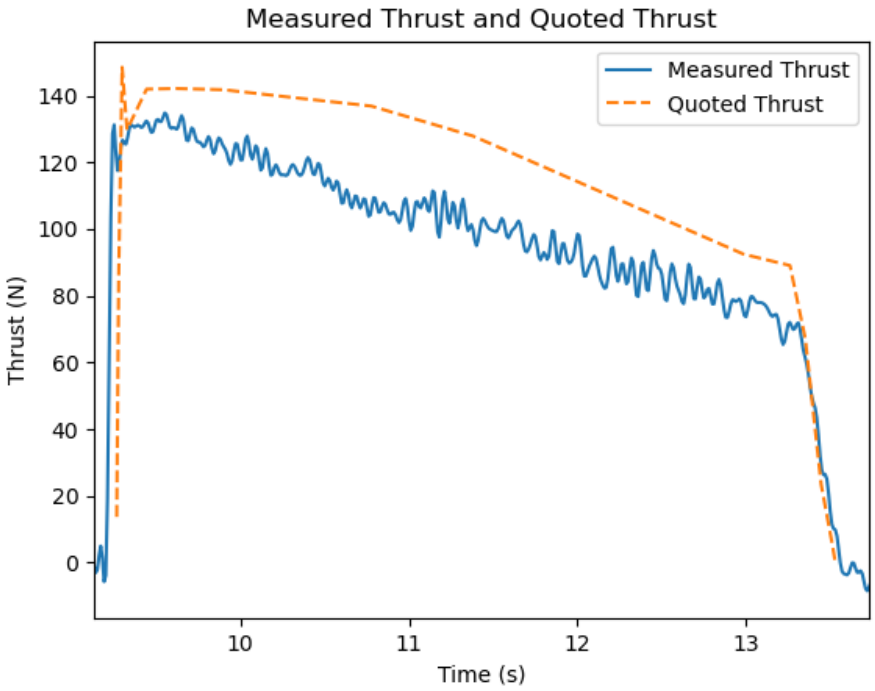

Fig. 13 Measured thrust during test plotted against quoted thrust from the manufacturer.

(a) Vane 1. **(b) Vane 2.**

(c) Vane 3. **(d) Vane 4.**

Fig. 14 Side views of all vanes post firing. Shaft on vane 4 was left in because set screw head had been eroded.

V. Conclusion and Future Work

In this work, we presented the design of a novel small-scale jet vane TVC concept which utilizes additive manufacturing to produce jet vanes that can perform in the demanding thermal and mechanical environment of a solid rocket motor exhaust stream. We also present extensive CFD and conjugate heat transfer simulation results evaluating the aerodynamic and thermodynamic performance of our jet vane designs. A TVC unit design which is suitable for integration into an autonomous MAV is also presented. In order to validate our simulations and to support continued refinement of our jet vane design, we also present design of a test stand which is capable of measuring the side forces and thrust force produced by a test article consisting of four of our TVC units and a commercial solid rocket motor. An initial test firing using this stand and our 3D-printed titanium jet vane design is performed in order to validate our simulations. We show that significant side forces are produced by our vane design.

In future work, we intend to perform additional tests to validate the silica sheath vane design and to investigate whether it offers any improvements to erosion and deformation of the vanes. Optimization of vane shape for maximum lift and minimum drag will also be performed, using the simulation framework we have developed as a starting point. Finally, other materials, such as Inconel, which are both commonly used to construct jet vanes and can now be additively manufactured will be investigated for our application.

References

[1] Helmy, S., and Helmy, A., "The Origins and Growth of Short Range Liquid Propellant Ballistic Rockets," *Propulsion and Energy Forum*, AIAA, 2020.

[2] Facciano, A. B., Seybold, K. G., Westberry-Kutz, T. L., and Widmer, D. O., "Evolved SeaSparrow Missile Jet Vane Control System Prototype Hardware Development," *AIAA Journal of Spacecraft and Rockets*, Vol. 39, No. 4, 2002, pp. 522–531.

[3] Sanders, A. D., Jenista, C. G., Gordon, S. E., Donnan, R. A., Goodman, J. M., Arrowood, R. H., Maschmeyer, T., Mavris, D. N., and Laughlin, B., "Multi-Disciplinary Design of a Supersonic, Long-Range, Air-Superiority Missile Through Parametric Design Space Exploration and Physics-Based Modeling," *AIAA/ASME/SAE/ASEE Joint Propulsion Conference*, 2014.

[4] Copenhagen Suborbitals, "Nexø II," `https://copenhagensuborbitals.com/missions/nexo-ii`, 2018.

[5] Nisser, M., Liao, C. C., Chai, Y., Adhikari, A., Hodges, S., and Mueller, S., "LaserFactory: A Laser Cutter-based Electromechanical Assembly and Fabrication Platform to Make Functional Devices & Robots," *Proceedings of the 2021 CHI Conference on Human Factors in Computing Systems*, Association for Computing Machinery, 2021.

[6] Bronz, M., Tal, E., Favalli, F., and Karaman, S., "Mission-Oriented Additive Manufacturing of Modular Mini-UAVs," *SciTech Forum*, AIAA, 2020.

[7] Danielson, A., "Inverse heat transfer studies and the effects of propellant aluminum TVC jet vane heating and erosion," *26th Joint Propulsion Conference*, AIAA, 1990.

[8] Rahaim, C., Cavalleri, R., McCarthy, J., and Kassab, A., "Jet vane thrust vector control - A design effort," *32nd Joint Propulsion Conference*, AIAA, 1996.

[9] Harrisson, V., deChamplain, A., Kretschmer, D., Farinaccio, R., and Stowe, R., "Force Measurements Evaluating Erosion Effects on Jet Vanes Thrust Vector Control System," *39th Joint Propulsion Conference*, AIAA, 2003.

[10] Sung, H.-G., and Hwang, Y.-S., "Thrust-Vector Characteristics of Jet Vanes Arranged in X-Formation Within a Shroud," *AIAA Journal of Propulsion and Power*, Vol. 20, No. 3, 2004, pp. 501–508.

[11] Lauzon, M., "5DOF dynamic loads on a jet vane," *26th Joint Propulsion Conference*, AIAA, 1990.

[12] "White Lightning Propellant Data Sheet," Tech. Rep. 8225W, 2021. URL `https://www.rocketmotorparts.com/54mm_White_Lightning__Propellant_Grain/p1577809_14677563.aspx`.

[13] Ponomarenko, A., "RPA: Tool for Liquid Propellant Rocket Engine Analysis C++ Implementation," 2010.

[14] Goodwin, D. G., Speth, R. L., Moffat, H. K., and Weber, B. W., *Cantera: An Object-oriented Software Toolkit for Chemical Kinetics, Thermodynamics, and Transport Processes*, 2021. https://doi.org/10.5281/zenodo.4527812, URL https://www.cantera.org.

[15] Hanson, B., *The Selection and Use of Titanium: A Design Guide*, Institute of Materials, Materials Information Service, 1995.